

# A microstructurally based continuum model of cartilage viscoelasticity and permeability incorporating measured statistical fiber orientations

David M. Pierce<sup>1</sup> · Michael J. Unterberger<sup>2</sup> · Werner Trobin<sup>3</sup> ·  
Tim Ricken<sup>4</sup> · Gerhard A. Holzapfel<sup>2</sup>

Received: 21 January 2015 / Accepted: 15 May 2015 / Published online: 23 May 2015  
© Springer-Verlag Berlin Heidelberg 2015

**Abstract** The remarkable mechanical properties of cartilage derive from an interplay of isotropically distributed, densely packed and negatively charged proteoglycans; a highly anisotropic and inhomogeneously oriented fiber network of collagens; and an interstitial electrolytic fluid. We propose a new 3D finite strain constitutive model capable of simultaneously addressing both solid (reinforcement) and fluid (permeability) dependence of the tissue's mechanical response on the patient-specific collagen fiber network. To represent fiber reinforcement, we integrate the strain energies of single collagen fibers—weighted by an orientation distribution function (ODF) defined over a unit sphere—over the distributed fiber orientations in 3D. We define the anisotropic intrinsic permeability of the tissue with a structure tensor based again on the integration of the local ODF over all spatial fiber orientations. By design, our modeling formulation accepts structural data on patient-specific collagen fiber networks as determined via diffusion tensor MRI. We implement our new model in 3D large strain finite elements and study the distributions of interstitial fluid pressure, fluid pressure load support and shear stress within a cartilage sample under indentation. Results show that the fiber network

dramatically increases interstitial fluid pressure and focuses it near the surface. Inhomogeneity in the tissue's composition also increases fluid pressure and reduces shear stress in the solid. Finally, a biphasic neo-Hookean material model, as is available in commercial finite element codes, does not capture important features of the intra-tissue response, e.g., distributions of interstitial fluid pressure and principal shear stress.

**Keywords** Cartilage · Constitutive modeling · Finite element simulation · Porous media · Collagen fiber · Diffusion tensor MRI

## 1 Introduction

Cartilage, a complex, multi-phase material, comprises (by percentage wet weight) fluid and electrolytes (68–85%), collagen fibers (15–25%), proteoglycans (5–10%) and chondrocytes (<0.01%) (Mow et al. 2005; Athanasiou et al. 2010). The predominantly type II collagen fibers exhibit a high level of structural organization usually consisting of three sub-tissue zones starting from the surface to the sub-chondral bone: The superficial zone has fibers which are predominantly tangential to the articular surface, the middle zone has fibers which are isotropically distributed and oriented, and the deep zone has fibers which are oriented predominantly perpendicular to the underlying bone (Mow et al. 2005; Pierce et al. 2013b). Mechanical properties of the solid phase derive from an interplay of isotropically distributed, densely packed and negatively charged proteoglycans (Hascall 1977; Muir 1983), and the highly anisotropic and inhomogeneously oriented fiber network of collagens. These two components also influence permeation of the fluid phase. The densely packed proteoglycans give an

✉ David M. Pierce  
dmpierce@engr.uconn.edu

<sup>1</sup> Departments of Mechanical Engineering, Biomedical Engineering and Mathematics, University of Connecticut, Storrs, CT, USA  
<sup>2</sup> Institute of Biomechanics, Graz University of Technology, Graz, Austria  
<sup>3</sup> Institute for Computer Graphics and Vision, Graz University of Technology, Graz, Austria  
<sup>4</sup> Mechanics-Statics-Dynamics, Faculty of Architecture and Civil Engineering, TU Dortmund University, Dortmund, Germany

extremely low permeability, while the collagenous fiber network gives an anisotropic and inhomogeneous permeability.

Diffusion tensor imaging (DT-MRI or DTI) is a magnetic resonance imaging (MRI) technique, which allows the microstructure of soft biological tissues, particularly cartilage, to be probed by determining the local mobility of water molecules, i.e., the local diffusivity characteristics (Basser et al. 1994). In fact, the anisotropic diffusion of water in cartilage, as captured by DT-MRI, reflects the general orientation of the collagen fibers within the network (Filidoro et al. 2005; Meder et al. 2006; Abdullah et al. 2007; de Visser et al. 2008a, b). Mathematically, this diffusion process can be formulated as a conditional probability density function  $P(\mathbf{x}, \mathbf{x}_0)$ , which specifies the probability of a water molecule to displace from its initial position  $\mathbf{x}_0$  to position  $\mathbf{x}$  in the given diffusion time  $\delta$  (e.g., in s). In classic DT-MRI, the averaged diffusion probabilities within a single voxel are modeled to be Gaussian, i.e., the diffusion propagator is given as

$$P(\boldsymbol{\xi}) = \left(4\pi b^{-1}\delta\right)^{-3/2} |\mathbf{D}|^{-1/2} \exp\left\{\frac{-b\boldsymbol{\xi}^T \mathbf{D}^{-1} \boldsymbol{\xi}}{4\delta}\right\}, \quad (1)$$

where  $\boldsymbol{\xi} = \mathbf{x} - \mathbf{x}_0$  is the relative molecule displacement (e.g., in mm),  $\mathbf{D}$  is the voxel's diffusion tensor (dimensionless) and  $b$  is the  $b$ -value used in the imaging protocol ( $\text{s}/\text{mm}^2$ ) (Basser et al. 1994; Price 2009; Pierce et al. 2010).

Despite the extreme complexity of the fundamental mechanisms underlying cartilage function, computational modeling can bring biological and medical data together with physics and engineering science into a patient-specific simulation environment. To facilitate finite element (FE) analysis of this complex soft tissue and hence further interdisciplinary studies, we propose a quasi-static, two-phase model with individually incompressible phases under isothermal conditions and without mass exchanges.

We model the proteoglycan solid as neo-Hookean and define a compaction point as the state in which all transportable fluid is pressed out of the tissue. To model mechanical contributions from the collagen fiber network, we integrate the strain energies of single collagen fibers—weighted by an orientation distribution function (ODF) defined over a unit sphere—over the distributed fiber orientations in 3D. We define the anisotropic intrinsic permeability of the cartilage solid matrix with a consistent spatial structural tensor based on the initial Darcy permeability, an isotropic deformation dependence, and again on the integration of the local ODF over all (normalized) spatial fiber orientations.

To increase the fidelity of our simulations, we define material parameters as constants and compositional parameters as functions of the normalized tissue thickness, and we use structural parameters to characterize local (element-wise) ODFs. We calibrate our model by fitting data from

the cartilage mechanics literature and determine the element-wise ODFs directly from sample-specific DT-MRI data. We specifically develop our modeling formulation to accept structural data on the patient-specific collagen fiber network as determined via DT-MRI (Pierce et al. 2010).

Several continuum constitutive models, based on ODFs and created for solids (and even cartilage), are proposed in the mechanics literature. Miehe et al. (2004) introduced a micro-mechanically motivated network model for the elastic response of rubbery polymers by homogenizing the response of microscopic free energies, oriented using a probability distribution function defined over a unit sphere, to determine the macroscopic total free energy. This model was subsequently extended to include the description of time-dependent viscoelastic effects (Miehe and Göktepe 2005). Particularizing ODFs to model distributions of collagen fibers, Topol et al. (2014) explored issues associated with ODFs for which the different fiber orientations at a given location may have different natural (stress-free) configurations.

Regarding the constitutive modeling of cartilage specifically, Lei and Szeri (2006) developed a 3D poroelastic model using arbitrary ODFs to realize structural anisotropy due to inhomogeneity in the distribution and orientation of fibers (while the permeability remained isotropic). The authors implemented their model in ABAQUS (Dassault Systèmes, Vélizy-Villacoublay, FR) using 2D axisymmetric elements, but never in 3D. Federico and Gasser (2010) proposed a constitutive model for biological tissues, which superposes elastic strain-energy potentials related to a matrix and a reinforcing continuous infinity of fiber families represented by a probability density function defined on the unit sphere. The authors modeled cartilage as a strictly incompressible, pure solid and used estimates for the material and structural parameters to demonstrate the constitutive model in 3D finite elements.

Ateshian et al. (2009) modeled the solid matrix of cartilage with a continuous fiber angular distribution, where fibers can only sustain tension, swelled by the osmotic pressure of a proteoglycan ground matrix. The authors particularized their constitutive model to focus on the tissue's equilibrium response to mechanical and osmotic loading, when flow-dependent and flow-independent viscoelastic effects have subsided; thus, they specialized the framework of triphasic theory for charged hydrated tissues to equilibrium conditions under finite deformation. This model is available for use in FEBio (Maas et al. 2012). In fact, several combinations of existing 3D multi-phasic constitutive models can be combined in a modular way using FEBio with constitutive equations for solute diffusivity and the mechanical effects of mechanochemical interactions (Maas et al. 2012). Tomic et al. (2014) implemented the model from Federico and Grillo (2012) into FEBio and exercised it modeling an unconfined compression test of articular cartilage. This

poroelastic constitutive model includes both an ODF describing statistically oriented fibers contributing to the elastic properties and an anisotropic permeability tensor obtained by upscaling the flow properties (Federico and Grillo 2012). Taffetani et al. (2014) generalized the angular distribution function proposed by Ateshian et al. (2009) and included this in a multi-constituent constitutive model that accounts for the nonlinear, porous and viscous aspects of cartilage. The authors implemented their constitutive model in ABAQUS and used 2D axisymmetric elements to simulate nanoindentation tests on cartilage.

Mechanisms for maximizing fluid pressure are important for normal tissue function because increased fluid pressure improves surface frictional properties (Ateshian et al. 1998), enhances load support and shields the solid matrix from load. In previous work (Pierce et al. 2013b), we tested the following hypotheses found in the cartilage mechanics literature: (1) the through-the-thickness structural arrangement of the collagen fiber fabric adjusts fluid permeation to maintain fluid pressure and optimize tissue function (Federico and Herzog 2008); (2) the inhomogeneity of mechanical properties through the cartilage thickness acts to maintain fluid pressure at the articular surface (Krishnan et al. 2003). To determine the effects of the collagen fiber network and through-the-thickness tissue inhomogeneity (of tissue constituents) independently, we selectively simplified our previous constitutive model by removing either the fiber network, or the tissue inhomogeneity, or both. Therein, we captured the anisotropic and nonlinear response of the dispersed collagen fiber fabric using a strain-energy function extended to consider the dispersion of the collagen fiber orientation (Gasser et al. 2006; Pierce et al. 2010). Furthermore, we assumed that each of the three sub-tissue zones was individually homogeneous, leading to a piecewise constant through-the-thickness description of both the fiber network and the model parameters. In that work, both through-the-thickness inhomogeneity of the collagen fiber distribution and of the material properties served to maintain fluid pressure, but depth-dependent model parameters appeared to have a larger effect on fluid pressure retention in the tissue sample, and on the advantageous pressure distribution (Pierce et al. 2013b).

In the present study, we implement our new constitutive formulation in 3D large strain finite elements and re-simulate the previous mechanical indentation tests to study the distributions of interstitial fluid pressure, fluid pressure load support and principal shear stress within the cartilage sample under indentation with a plane-ended, 1 mm diameter cylindrical indenter. With our new model, we have improved the representation of both the collagen fiber network and the depth-dependent tissue composition (varies continuously). To demonstrate our new constitutive model, we retest our original hypotheses. Our results show that the fiber network

dramatically increases interstitial fluid pressure and focuses it near the surface tissue. Inhomogeneity in the tissue's composition also increases fluid pressure, although to a lesser extent than the fiber network, and also reduces principal shear stress in the solid. Finally, a biphasic neo-Hookean material model, as is available in commercial FE codes, does not capture important features of the intra-tissue response, e.g., distributions of interstitial fluid pressure and principal shear stress.

## 2 Constitutive model

Our constitutive model is based on four main assumptions. First, we assume that the cartilage tissue consists of two phases: a porous solid skeleton saturated by a pore fluid. This assumption implies that under physiologic loading conditions, the magnitude of the swelling strain due to Donnan osmotic pressure (resulting from changes in the total ion concentration of the tissue) is relatively small in comparison with the tissue strains, so that we are justified in approximating the physiologic response using a biphasic model (Soltz and Ateshian 2000). Second, we assume that both phases are individually incompressible, see, e.g., (Jurvelin et al. 1997; Bachrach et al. 1998; Soltz and Ateshian 1998; Wong et al. 2000; Humphrey 2002; Park et al. 2003; Huang et al. 2005). Our third assumption is that mass exchanges between the solid and the fluid constituents can be neglected (immiscibility). Finally, we assume that dynamic effects are negligible (quasi-static), so we restrict both phases to exclude inertial terms.

We describe articular cartilage as a biphasic continuum  $\varphi = \varphi^S + \varphi^F$ , which consists of a porous solid phase  $\varphi^S$  saturated with the fluid phase  $\varphi^F$ , the latter representing the interstitial water. The solid phase represents an incompressible tissue with an isotropic and statistically regular pore distribution and with an imbedded reinforcing collagen fiber network. To describe this biphasic system, we use the theory of porous media within a superimposed, continuum mechanical framework, see e.g., Bowen (1980, 1982), Ehlers (1989, 1993), de Boer (2000) and Pence (2012).

We represent the microscopic tissue structure with a statistical distribution of the constituents over a representative elementary volume by their average volume fractions  $n^\alpha$ . The volume fractions  $n^\alpha$  refer the volume elements  $dv^\alpha$  of the individual constituents  $\varphi^\alpha$  to the bulk volume element  $dv$  with

$$n^\alpha(\mathbf{x}, t) = \frac{dv^\alpha}{dv},$$

$$\sum_{\alpha=1}^k n^\alpha(\mathbf{x}, t) = \sum_{\alpha=1}^k \frac{\rho^\alpha}{\rho^{\alpha R}} = 1, \quad \alpha \in \{S, F\}, \quad (2)$$

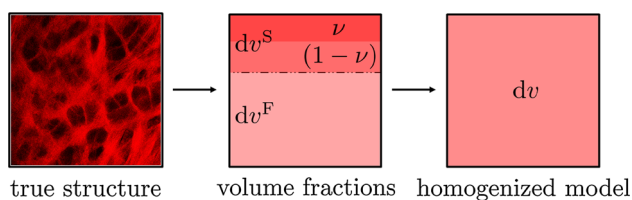


**Fig. 1** Schematic representation of the true cartilage structure (multi-photon microscopy image), its representation using volume fractions and the corresponding homogenization within the theory of porous media

where  $\mathbf{x}$  is the position vector of the spatial point (reference position  $\mathbf{X}$ ),  $t$  is the time, and S and F denote the solid and fluid, respectively. The volume fractions  $n^\alpha$  in (2)<sub>1</sub> satisfy the saturation condition (2)<sub>2</sub> for  $k$  constituents  $\varphi^\alpha$ . Moreover, the partial density  $\rho^\alpha = n^\alpha \rho^{\alpha R}$  of the constituent  $\varphi^\alpha$  is related to the real density of the materials  $\rho^{\alpha R}$  involved via the volume fractions  $n^\alpha$ , see (2)<sub>2</sub>. We further partition the solid volume increment  $dv^S$  into the volume fraction of fiber network  $\nu$  relative to total solid and that of isotropic matrix  $(1 - \nu)$ . See Fig. 1 for a schematic representation of the constitutive modeling approach, illustrating the true cartilage structure, its representation using volume fractions and the corresponding homogenization within the theory of porous media. For an extended explanation of the kinematics of porous media, see de Boer (2000) or Ehlers (2002).

**2.1 Fluid and elastic solid contributions to the stress**

We propose the constitutive relation for the total Cauchy stress tensor as

$$\boldsymbol{\sigma} = -p \mathbf{I} + 2 \rho^S \mathbf{F}_S \frac{\partial \Psi^S}{\partial \mathbf{C}_S} \mathbf{F}_S^T = -p \mathbf{I} + \boldsymbol{\sigma}_E^S, \tag{3}$$

where  $p$  is the fluid pressure,  $\mathbf{I}$  is the second-order identity tensor,  $\mathbf{F}_S = \partial \mathbf{x}_S / \partial \mathbf{X}_S$  is the deformation gradient of the solid,  $\mathbf{C}_S = \mathbf{F}_S^T \mathbf{F}_S$  is the right Cauchy–Green tensor and  $\boldsymbol{\sigma}_E^S$  is the effective Cauchy stress tensor, see e.g., Bishop (1959) or Skempton (1960).

We use an additive decomposition of the superimposed solid Helmholtz free-energy function  $\Psi^S$  into an isotropic matrix part  $\Psi_{IM}^S$ , and a transversely isotropic fiber network part  $\Psi_{FN}^S$  as

$$\Psi^S = (1 - \nu) \Psi_{IM}^S (J_S, I_1) + \nu \Psi_{FN}^S (\mathbf{C}_S), \tag{4}$$

where  $\nu$  is the volume fraction of the collagen fiber network to the total solid,  $J_S = \det \mathbf{F}_S$  is the Jacobian and  $I_1 = \text{tr} \mathbf{C}_S$  is the first invariant of  $\mathbf{C}_S$ .

In the case of volumetric compression, a compaction point must be introduced defining the state where no further compression can occur, i.e., all fluid is pressed out of the tissue,

and all pores are closed, see e.g., Wilson et al. (2007) and Federico and Grillo (2012). We use a strain-energy function based on Simo and Pister (1984) to capture the response of the isotropic (largely) proteoglycan solid matrix, which has been extended to include compaction effects as (Bluhm 2002; Pierce et al. 2013a, b)

$$\Psi_{IM}^S (J_S, I_1) = \frac{1}{\rho_{0S}^S} \left[ U(J_S) + \frac{1}{2} \mu^S (I_1 - 3) \right], \tag{5}$$

where

$$U(J_S) = \chi_{cp}^S \left[ \frac{1}{2} (\log J_S)^2 + \zeta^S \right] - \mu^S \log J_S, \tag{6}$$

and where we use the abbreviations

$$\begin{aligned} \chi_{cp}^S &= \lambda^S \left[ 1 + J_{cp}^S \left( 1 + \frac{(J_{cp}^S)^2}{1 - J_{cp}^S} \right) \right]^{-1}, \\ \zeta^S &= J_{cp}^S \log J_S + \frac{1 - J_{cp}^S}{J_{cp}^S - 2} \\ &\times \left[ \log \frac{J_{cp}^S - J_S}{J_S (J_{cp}^S - 1) - J_{cp}^S} - \log (1 - J_{cp}^S) \right]. \end{aligned} \tag{7}$$

In (5)–(7)  $\mu^S$  is Lamé’s second parameter (a stress-like material parameter corresponding to the shear modulus of the underlying matrix in the reference configuration),  $\lambda^S$  is Lamé’s first parameter (a stress-like material parameter, which degenerates to a non-physical, (positive) penalty parameter used to enforce incompressibility, cf. Pence 2012), and  $n_{0S}^S \leq J_{cp}^S \leq 1$  defines the point of compaction for the tissue, where  $n_{0S}^S$  is the solid volume fraction in the reference configuration and it is generally not possible to “squeeze out” all of the fluid from the tissue.

To capture the anisotropic and nonlinear response of the dispersed collagen fiber network, suppose that a distribution of fibers is embedded in this isotropic matrix, and that each fiber deforms with the matrix. Let  $\rho(\mathbf{M})$  be the angular density of fibers (the ODF) so that (Miehe et al. 2004; Lei and Szeri 2006)

$$\frac{1}{4\pi} \int_{\Omega} \rho(\mathbf{M}) \, d\Omega = 1, \tag{8}$$

where  $\Omega = \mathbf{M} \in \mathbb{R}^3 : |\mathbf{M}| = 1$  is the unit sphere.

For a single fiber of reference angular orientation  $\mathbf{M}$ , the fourth pseudo-invariant  $I_4$  is the square of the stretch of this fiber in the direction  $\mathbf{m} = \mathbf{F}_S \mathbf{M}$ , i.e.,  $I_4(\mathbf{M}) = \lambda^2(\mathbf{M}) = \mathbf{M} \cdot \mathbf{C}_S \mathbf{M}$ . We define the strain energy of a single collagen fiber as (Holzapfel et al. 2000)

$$w(I_4) = \frac{k_1}{2k_2} \left\{ \exp[k_2(I_4 - 1)^2] - 1 \right\} \mathcal{H}(I_4 - 1), \tag{9}$$

where  $k_1 > 0$  is a stress-like material parameter,  $k_2 > 0$  is a dimensionless parameter and  $\mathcal{H}$  is a Heaviside step function evaluated at  $(I_4 - 1)$ , i.e., the collagen fibers only engage under stretches greater than unity. The form of this strain-energy function is based on the experimentally supported assumption that energy is required to straighten a (wavy) collagen fiber, and that once straightened, a fiber has a strong stiffening response under tension, cf. Sun et al. (2002).

The strain energy in the increment  $d\Omega$  is thus  $\rho(\mathbf{M})w(I_4) d\Omega$ . Assuming that all of the collagen fibers have the same properties, i.e., the same form for  $w(I_4)$ , we calculate the total strain-energy function (over all orientations) as

$$\Psi_{\text{FN}}(\mathbf{C}, \mathbf{M}) = \frac{1}{\rho_{0S}^S} \int_{\Omega} \rho(\mathbf{M})w(I_4) d\Omega. \tag{10}$$

Within the FE method, we evaluate such integrals numerically following the method suggested by Bažant and Oh (1986) (see ‘Appendix 1’ for details). The formulation can readily be generalized to account for different types of collagen fibers, cf. Sáez et al. (2012) and Holzapfel et al. (2014).

### 2.2 Viscoelasticity of the solid constituents

We calculate the viscous contribution to the total stress state in the Lagrangian configuration using the second Piola–Kirchhoff effective stress tensor  $\mathbf{S}_E^S = J_S \mathbf{F}_S^{-1} \sigma_E^S \mathbf{F}_S^{-T}$  of the solid. For clarity in what follows, we drop the superscript S and the subscript E and denote the second Piola–Kirchhoff effective stress tensor of the solid by  $\mathbf{S}$ . We specify the second Piola–Kirchhoff effective stress by summing the matrix, fiber network and viscoelastic contributions as

$$\mathbf{S} = \sum_{\gamma=\text{IM, FN}} (\mathbf{S}_{\gamma} + \mathbf{Q}_{\gamma}), \tag{11}$$

where  $\mathbf{S}_{\text{IM}} = 2\rho_{0S}^S \partial \Psi_{\text{IM}} / \partial \mathbf{C}_S$  is the matrix, and  $\mathbf{S}_{\text{FN}} = 2\rho_{0S}^S \partial \Psi_{\text{FN}} / \partial \mathbf{C}_S$  is the fiber network contribution to the second Piola–Kirchhoff effective stress  $\mathbf{S}$ , respectively, and  $\mathbf{Q}_{\gamma}$  represent the viscoelastic contributions where we assume  $\gamma \in \{\text{IM}, \text{FN}\}$  time-dependent processes.

To determine the time-dependent (viscous) response of the matrix and the fiber network, we consider a partition of the closed time interval  $t \in [0^+, T]$  and focus attention on a typical time subinterval  $[t_n, t_{n+1}]$ , with  $\Delta t = t_{n+1} - t_n$  characterizing the associated *time increment*, cf. Herrmann and Peterson (1968), Taylor et al. (1970), Simo (1987) and Holzapfel (1996). Assume now that at times  $t_n$  and  $t_{n+1}$  all relevant kinematic quantities are given, and that the stress  $\mathbf{S}_n$  at time  $t_n$  is also specified uniquely via the associated constitutive equation.

All that remains is the computation of the second Piola–Kirchhoff stress tensor  $\mathbf{S}_{n+1}$  at time  $t_{n+1}$  [the algorithmic stress tensor generalized from (11)], which we calculate as

$$\mathbf{S}_{n+1} = \sum_{\gamma=\text{IM, FN}} (\mathbf{S}_{\gamma, n+1} + \mathbf{Q}_{\gamma, n+1}). \tag{12}$$

The stress contributions  $\mathbf{S}_{\text{IM}, n+1}$  and  $\mathbf{S}_{\text{FN}, n+1}$  describe the total elastic response computed from the given strain measures at  $t_{n+1}$ . The terms  $\mathbf{Q}_{\gamma, n+1}$  in (12) represent the non-equilibrium stresses at time  $t_{n+1}$ .

We assume that the transient behaviors, introduced by  $\mathbf{Q}_{\gamma}$  in (11), satisfy the evolution equations

$$\dot{\mathbf{Q}}_{\gamma} + \frac{\mathbf{Q}_{\gamma}}{\tau_{\gamma}} = \beta_{\gamma} \dot{\mathbf{S}}_{\gamma}, \tag{13}$$

where the dot denotes the material time derivative,  $\beta_{\gamma}$  is a dimensionless strain-energy factor controlling the magnitude of the viscous component response and  $\tau_{\gamma}$  is the associated relaxation time. Using the *mid-point rule*, we arrive at a second-order accurate *recurrence update formula* for the non-equilibrium stresses as

$$\mathbf{Q}_{\gamma, n+1} = \beta_{\gamma} \exp(-\Delta t / 2\tau_{\gamma}) \mathbf{S}_{\gamma, n+1} + \mathcal{H}_{\gamma, n}, \tag{14}$$

with

$$\mathcal{H}_{\gamma, n} = \exp(-\Delta t / 2\tau_{\gamma}) \times [\exp(-\Delta t / 2\tau_{\gamma}) \mathbf{Q}_{\gamma, n} - \beta_{\gamma} \mathbf{S}_{\gamma, n}]. \tag{15}$$

We determine the algorithmic history term  $\mathcal{H}_{\gamma, n}$ ,  $\gamma \in \{\text{IM}, \text{FN}\}$ , at time  $t_n$ , from the known stresses  $\mathbf{Q}_{\gamma}$  and  $\mathbf{S}_{\gamma}$  at  $t_n$  (for numerical purposes, we have assumed  $\mathbf{Q}_{\gamma}^{0+} = \mathbf{0}$ ), see Holzapfel (1996), Holzapfel and Gasser (2001). At thermodynamical equilibrium,  $\mathbf{Q}_{\gamma} = \mathbf{0}$ , which means that only the elastic response remains.

### 2.3 Corresponding permeability

The diffusion of interstitial fluid within cartilage, as visualized, e.g., by DT-MRI, is principally influenced by the general orientation of the (largely type II) collagen fibers (Filidoro et al. 2005; Meder et al. 2006; Abdullah et al. 2007; de Visser et al. 2008a, b). In short, the presence of the collagen fibers restricts the diffusion of interstitial fluid within cartilage, leading to a correspondingly higher diffusivity in directions parallel to local fiber orientations.

In order to use a material objective measure of the fluid velocity with respect to the solid velocity, we introduce the seepage velocity  $\mathbf{w}_{\text{FS}}$ , which describes the difference in velocity between the fluid phase  $\mathbf{x}'_{\text{f}}$  and the solid phase  $\mathbf{x}'_{\text{s}}$  as

$\mathbf{w}_{\text{FS}} = \mathbf{x}'_{\text{F}} - \mathbf{x}'_{\text{S}}$ . We determine the filtration velocity  $n^{\text{F}} \mathbf{w}_{\text{FS}}$  as [cf. Pierce et al. (2013a, 2013b)]

$$n^{\text{F}} \mathbf{w}_{\text{FS}} = \left(n^{\text{F}}\right)^2 \mathbf{R}_{\text{F}}^{-1} \left(-\text{grad } p + \rho^{\text{FR}} \mathbf{b}\right), \quad (16)$$

where  $\mathbf{R}_{\text{F}}$  is a positive-definite material parameter tensor representing the intrinsic hydraulic resistance of the cartilage solid matrix and  $\mathbf{b}$  is the body force per unit mass. We propose the anisotropic intrinsic permeability of the cartilage solid matrix  $\mathbf{K}_{\text{F}}$  as (cf. Ricken and Bluhm 2010; Pierce et al. 2013a)

$$\mathbf{K}_{\text{F}} = \left(n^{\text{F}}\right)^2 \mathbf{R}_{\text{F}}^{-1} = k_{0\text{S}} \left(\frac{n^{\text{F}}}{1 - n_{0\text{S}}^{\text{S}}}\right)^m \mathbf{H}, \quad (17)$$

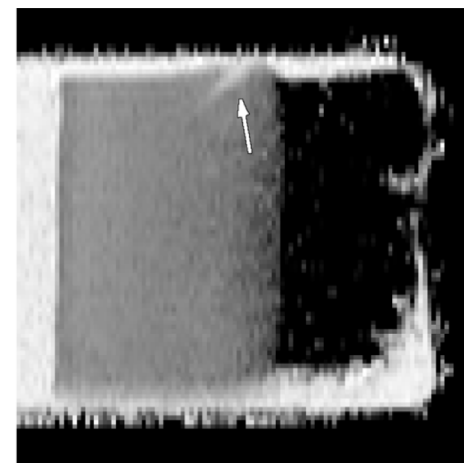
$$\mathbf{H} = \frac{1}{4\pi} \int_{\Omega} \frac{\rho(\mathbf{M})}{I_4(\mathbf{m})} \mathbf{m} \otimes \mathbf{m} \, d\Omega,$$

where  $\mathbf{H}$  is a spatial structure tensor defined by the integration of  $\rho(\mathbf{M})$  over all (normalized) spatial fiber orientations  $\hat{\mathbf{m}} = \lambda^{-1} \mathbf{F}_{\text{S}} \mathbf{M}$  (with  $\lambda = |\mathbf{m}|$ ),  $k_{0\text{S}}$  [ $\text{m}^4/\text{Ns}$ ] is the initial Darcy permeability and  $m$  is a dimensionless parameter controlling the general isotropic deformation dependence of the permeability, see also, e.g., Eipper (1988). Inclusion of the volume fraction  $n^{\text{F}}$  relates to the change of permeability caused by the change of pore space, where  $n_{0\text{S}}^{\text{S}}$  denotes the reference solid volume fraction. Here we use  $\mathbf{H}$ , via  $\rho(\mathbf{M})$ , to define the range of permeabilities resulting from ideal alignment of collagen fibers to an isotropic distribution of the collagen fibers.

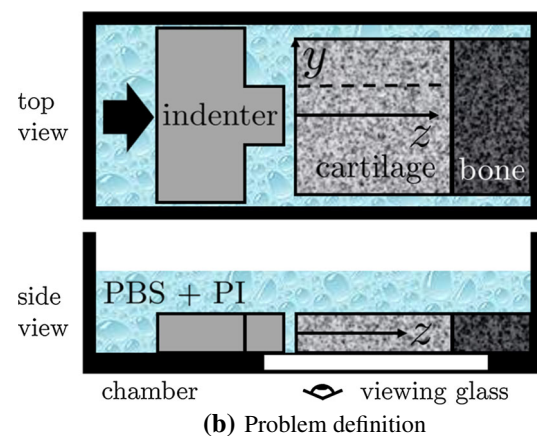
### 3 Methods: representative example

#### 3.1 DT-MRI experiment

We use DT-MRI data generated in our previous work (Pierce et al. 2010), which we briefly outline here for completeness. Previously we harvested the left patella of a healthy 27-year-old male within 24 h from death and stored it in physiologic solution for 36 h at 4 °C. Prior to MRI examination we cut a cuboid sample from the central part of the lateral facet of the patellar cartilage. The sample fit into a glass vessel of 4 mm internal diameter which, in turn fit tightly into a 5 mm birdcage coil used for the MRI experiments. The cuboid sample constitutes  $\sim 2.8 \times 2.8 \times 2.6$  mm in cartilage, and another  $\sim 1$  mm in bone thickness, to ensure that the corners of the sample serve to fix it within the glass vessel. We performed the MRI experiments with a 17.6 T scanner (UltraStabilized magnet system, Bruker BioSpin, Rheinstetten, Germany) using a one channel 5 mm birdcage coil provided by the manufacturer. We immersed the sample and vessel in physiologic solution maintained at 17–19 °C and imaged the assembly



(a) DT-MRI



(b) Problem definition

**Fig. 2** a Grayscale representation of the first principal eigenvalues of the DT-MRI data, a small fissure close to the cartilage-bone transition is indicated by the *white arrow* (Pierce et al. 2010). Principal diffusion in water is represented using *white voxels*, while regions with negligible water content are represented as *black voxels*. Intermediate values span the range from *black* to *white*; b schematic diagram of a near 2-D indentation test replicating the intra-tissue deformation that occurs during 3D indentation with a plane-ended cylindrical indenter, where PBS + PI indicates Phosphate Buffered Saline plus Protease Inhibitors (adapted from Bae et al. 2006)

through the cartilage thickness and diagonal to the square footprint in order to maximize the imaged volume. The total acquisition time of the DT-MRI experiment is  $\sim 140$  min. For more details on the MRI experiments and protocols refer to Pierce et al. (2010), Raya et al. (2011, 2013).

#### 3.2 Implementation of DT-MRI data

The measurement process outlined above yields a set of diffusion-weighted images, which enable us to reconstruct a voxel grid of diffusion tensors for the imaged volumetric slice. Figure 2a depicts the first principal eigenvalues of the tensor field, the rectangular gray area is the articular car-

tilage layer and the noisy black area directly below is the subchondral bone (Pierce et al. 2010). The cartilage-bone sample is surrounded by water (solid white, representing a higher diffusivity) and is enclosed in a cylindrical container (solid black border). Based on this data we infer the sample-specific geometric boundaries as well as the fiber distribution in the cartilage region. To remain consistent with our previous work (Pierce et al. 2010), we follow the same procedure to obtain a structured FE mesh: we first locate the geometric boundaries as sub-voxel-accurate zero-crossings of the second spatial derivative (Laplacian of Gaussian filter), then we use the voxel grid from the DT-MRI experiment as structured mesh. Along the boundaries of the cartilage region we use a semiautomatic process to transition from the structured voxel grid to the natural cartilage boundary while maintaining good element aspect ratios. Finally, the obtained 2D mesh is extruded to generate a 3D mesh of 20-node brick elements, representing the volume of the imaged DT-MRI slice.

By construction, one tensor per element is available within the ‘inner’ regions of the mesh, i.e., there is a one-to-one mapping from diffusion tensors to elements. Due to geometrical constraints on the FE mesh, this one-to-one mapping breaks down along the boundary. For every element in these ‘outer’ regions of the mesh we perform a weighted interpolation of the element’s four nearest diffusion tensors in the voxel grid using a Log-Euclidean framework (Arsigny et al. 2006).

Recalling from the introduction that the directional diffusion properties of water in cartilage are induced by the orientation of the collagen fibers, the element-wise tensor data naturally maps to the model’s ODF for the fiber network. We first convert the diffusion probability density function (1) to spherical coordinates  $(r, \theta, \phi)$ , then marginalize out the radius  $r$  (see ‘Appendix 3’ for details). An analytical form of the required ODF results as

$$\rho(\mathbf{M}, \mathbf{D}) = \frac{\sin \theta}{|\mathbf{D}|^{1/2} (\mathbf{M}^T \mathbf{D}^{-1} \mathbf{M})^{3/2}}, \tag{18}$$

where  $\mathbf{M} = (\cos \theta \sin \phi, \sin \theta \sin \phi, \cos \phi)^T$  and  $\mathbf{D}$  is the symmetric, positive-definite diffusion tensor for a specific element. The factor  $\sin \theta$  is introduced by the change from Cartesian to spherical variables to account for the fact that the surface element on the sphere is not uniform across the entire domain.

### 3.3 Material, compositional and structural parameters

Table 1 gives a summary of the required material, compositional and structural parameters—values used to approximate the response of the human patellar cartilage through the tissue thickness—and corresponding units, c.f. Pierce et al. (2013a, 2013b).

**Table 1** Required material, compositional and structural parameters—values used to approximate the response of the human patellar cartilage through the tissue thickness—and corresponding units

		Unit
<i>Material parameter</i>		
$\rho^{\text{FR}}$	$9.9 \times 10^2$	kg/m <sup>3</sup>
$\rho^{\text{SR}}$	$1.5 \times 10^3$	kg/m <sup>3</sup>
$\mu^{\text{S}}$	$2.3 \times 10^5$	N/m <sup>2</sup>
$k_1, k_2$	$4.3 \times 10^5, 40$	N/m <sup>2</sup> , –
$\beta_{\text{IM}}, \tau_{\text{IM}}$	1.0, 1	–, s
$\beta_{\text{FN}}, \tau_{\text{FN}}$	2.2, 100	–, s
<i>Compositional parameter</i>		
$n_{0\text{S}}^{\text{S}}(z^*)$	$0.15 + 0.15(z^*)$	–
$\nu(z^*)$	$0.43(z^*)^2 - 0.60(z^*) + 0.85$	–
$J_{\text{cp}}^{\text{S}}(z^*)$	$0.36 + 0.11(z^*)$	–
$k_{0\text{S}}(z^*)$	$1 \times 10^{-15} - 0.9 \times 10^{-15}(z^*)$	m <sup>4</sup> /Ns
$m(z^*)$	$3.0 + 5.0(z^*)$	–
<i>Structural parameter</i>		
<b>D</b>	DT-MRI	–

The parameter  $z^* \in [0, 1]$  is the normalized tissue thickness, where zero refers to the articular surface and one refers to the interface with subchondral bone. Note that the structural parameter **D** for the orientation distribution function  $\rho(\mathbf{M}, \mathbf{D})$  is determined directly from DT-MRI data for the specific sample analyzed, as discussed in the Sect. 3.2

Material parameters are intrinsic to the properties of the tissue constituents. Here we specify  $\rho^{\text{FR}}$  as the mass density of water at 37.1 °C and calculate  $\rho^{\text{SR}}$  using data from Bassler et al. (1998). We specify the average equilibrium shear modulus  $\mu^{\text{S}}$  of patellar cartilage based on the cartilage mechanics literature (Zhu et al. 1986, 1993; Mow et al. 2005). To specify the stiffening response of a single collagen fiber, i.e.,  $k_1$  and  $k_2$ , we draw on the work of García and Cortés (2007), Pierce et al. (2009). In light of the lack of direct data on the viscoelastic response of the proteoglycan matrix and the type II collagen fibers individually, we estimate  $\beta_{\text{IM}}$  based on unpublished experience with experiments and specify  $\beta_{\text{FN}}$  using data from Li and Herzog (2004). We infer from the literature that the parameters  $\tau_{\text{IM}}$  and  $\tau_{\text{FN}}$  must lie in the range  $0.21\text{--}1.03 \text{ s} \sim \tau_{\text{IM}} < \tau_{\text{f}} \sim 40\text{--}675 \text{ s}$  (DiSilvestro and Suh 2001; Charlebois et al. 2004; García and Cortés 2007; Pierce et al. 2009).

Compositional parameters refer to the local distribution of constituents within the tissue. Following the approach from Wilson et al. (2007), we specify compositional parameters as functions of the local, normalized tissue thickness  $z^* \in [0, 1]$ , where  $z^* = 0$  refers to the articular surface and  $z^* = 1$  refers to the interface with the subchondral bone. We specify the reference solid volume fraction  $n_{0\text{S}}^{\text{S}}(z^*)$  based on data from Mow et al. (2005). To determine the volume fraction of the collagen fiber network to the total solid  $\nu(z^*)$  we

fit data from both Mow et al. (2005) and Athanasiou et al. (2010). Lacking experimental data we assume a linear distribution for the point of compaction for the solid  $J_{cp}^S(z^*)$  and follow arguments from Pierce et al. (2013b). To determine the initial Darcy permeability  $k_{0S}(z^*)$  we assume a linear relationship and fit data from Krishnan et al. (2003) which we (slightly) adjust to data ranges from Mow et al. (2005). Similarly, we assume a linear relationship for the parameter controlling the general isotropic deformation dependence of the permeability  $m(z^*)$  based on data from both Chen et al. (2001) and Mow et al. (2005). Finally, we determine the structural parameter  $\mathbf{D}$  required for the ODF  $\rho(\mathbf{M}, \mathbf{D})$  directly from DT-MRI data on the specific sample analyzed, as discussed in the Sect. 3.2.

### 3.4 Finite element simulations

We perform ‘near’ 2-D indentation tests to study the intra-tissue Green–Lagrange strain, interstitial fluid pressure, principal shear stress and fluid pressure load support distributions resulting in the cartilage sample due to indentation with a plane-ended, 1 mm diameter cylindrical indenter, cf. Pierce et al. (2013b). Following Bae et al. (2006), a vertical bisection during 3D indentation of the cartilage surface using a plane-ended cylinder would reveal rectangular cut-planes for both the indenter and the sample. Therefore, an indentation test using the simpler geometry of a rectangular prismatic tip compressing a rectangular sample, with a constrained side to prevent out-of-plane motion, would exhibit the main features of intra-tissue deformation in the 3D counterpart (Bae et al. 2006), cf. Fig. 2b.

To model the test setup, we fix all displacement degrees of freedom for nodes coincident with the subchondral bone interface, and set the corresponding fluid flux normal to this surface to zero. We apply symmetry boundary conditions to both cross-sectional surfaces of the tissue, one side representing the imaging plane of the experimental setup and the other resulting from the relative thickness of the FE model. At the contact interface with the impermeable indenter (at the left surface in Fig. 2a) we prescribe the axial surface displacement to cause 1 % global tissue strain in 150 s and set the corresponding fluid flux normal to this interface to zero. We specify all remaining nodes in contact with the physiological solution as free to displace and set the corresponding fluid pressure to zero.

To study the effects of the collagen fiber network and through-the-thickness tissue inhomogeneity (of mechanical properties) independently, we follow the methodology of our previous work (Pierce et al. 2013b) and complete finite deformation contact simulations of the indentation experiment using four models—Model 1: patient-specific collagen fiber network, inhomogeneous compositional parameters; Model 2: patient-specific collagen fiber network, homoge-

neous compositional parameters; Model 3: no collagen fiber network, inhomogeneous compositional parameters; and Model 4: no collagen fiber network, homogeneous compositional parameters. Models with inhomogeneous compositional parameters use the through-the-thickness parameters, as detailed in Table 1, while homogeneous models use constant mean parameters throughout the entire mesh. We define the fluid pressure load support  $R_i^F$  at a tissue point in the  $i$ -direction as  $R_i^F = -p/(-p + (\sigma_E^S)_{ii})$ , i.e., pressure divided by the total normal stress, where  $(\sigma_E^S)_{ii}$  is the  $ii$ -component of the effective solid Cauchy stress tensor (Pierce et al. 2013a, b).

Each simulation employs 1938 20-node hexahedral elements of the Taylor–Hood type, with quadratic shape functions for solid displacements and bilinear shape functions for saturation pressure. We complete all simulations in the FE program ParFEAP (University of California at Berkeley, CA, United States) using a total Lagrangian formulation and the included Newton–Raphson algorithm. To implement the constitutive equations, we require elasticity tensors for both the isotropic matrix and fiber network contributions to the solid extra stress as well as the derivative of the filtration velocity  $n^F \mathbf{w}_{FS}$  with respect to both the deformation gradient  $\mathbf{F}_S$  and the material gradient of the interstitial fluid pressure  $\text{grad } p$  (see ‘Appendix 2’ for details on the last).

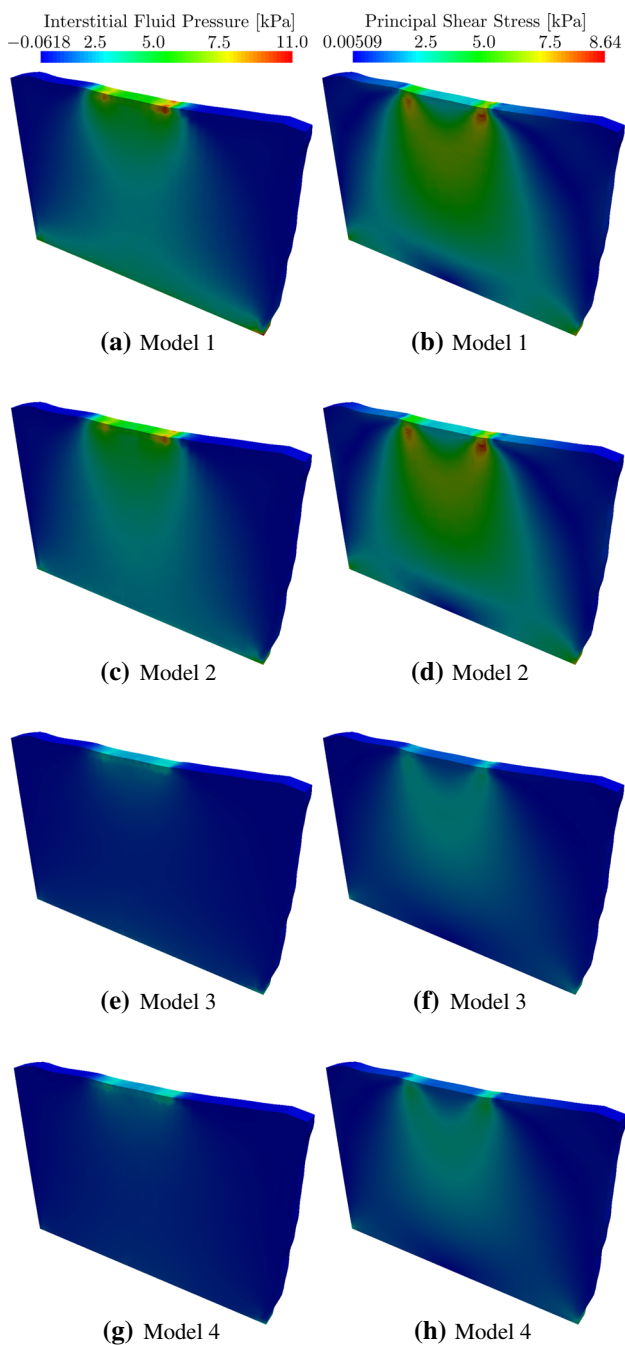
## 4 Results

Figure 3 depicts simulation results for the indentation experiment with an impermeable, plane-ended cylinder of diameter 1 mm compressing the cartilage sample to 1 % global strain in 150 s. Specifically, the first [(a), (c), (e), (g)] and second [(b), (d), (f), (h)] columns depict the interstitial fluid pressure and the principal (maximum) shear stress, respectively. As for the rows, Row 1 [(a), (b)] corresponds to Model 1—patient-specific collagen fiber network, inhomogeneous compositional parameters; Row 2 [(c), (d)]: Model 2—patient-specific collagen fiber network, homogeneous compositional parameters; Row 3 [(e), (f)]: Model 3—no collagen fiber network, inhomogeneous compositional parameters; and Row 4 [(g), (h)]: Model 4—no collagen fiber network, homogeneous compositional parameters.

Figure 4 depicts simulation results plotted along the  $z$ -axis in Fig. 2b, i.e., through the tissue thickness along the main axis of the indenter, for the indentation experiment. Specifically, Fig. 4(a) depicts the interstitial fluid pressure; (b) the principal shear stress; and (c) the fluid pressure load support; where Models 1, 2, 3 and 4 are consistent with the earlier descriptions in this section.

Figure 5 depicts simulation results plotted along the dashed line in Fig. 2b, i.e., through the tissue thickness at the edge of the indenter, for the indentation experiment. Similarly, Fig. 5(a) depicts the interstitial fluid pressure; (b) the





**Fig. 3** Simulation results for the indentation experiment with an impermeable, plane-ended cylinder of diameter 1 mm compressing the cartilage sample to 1% global strain in 150s. *Column 1* interstitial fluid pressure; *Column 2* principal shear stress. *Row 1* Model 1 (patient-specific collagen fiber network, inhomogeneous compositional parameters); *Row 2* Model 2 (patient-specific collagen fiber network, homogeneous compositional parameters); *Row 3* Model 3 (no collagen fiber network, inhomogeneous compositional parameters); *Row 4* Model 4 (no collagen fiber network, homogeneous compositional parameters)

principal shear stress; and (c) the fluid pressure load support; where again Models 1, 2, 3 and 4 are consistent with the earlier descriptions.

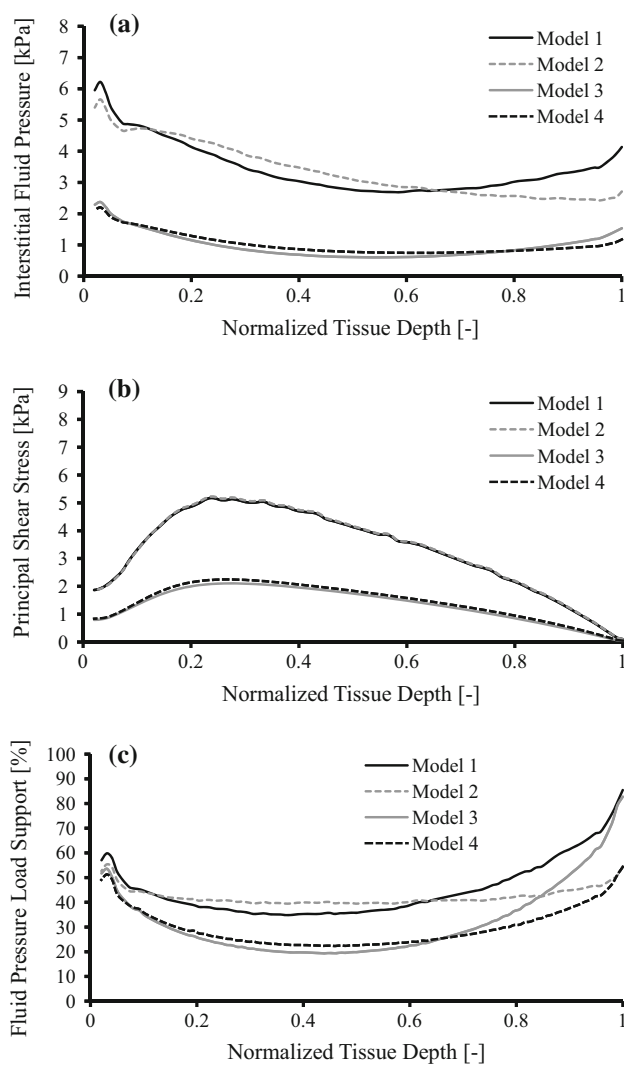


**Fig. 4** Simulation results plotted along the  $z$ -axis in Fig. 2b, i.e., through the tissue thickness along the main axis of the indenter, for the indentation experiment with an impermeable, plane-ended cylinder of diameter 1 mm compressing the cartilage sample to 1% global strain in 150s: **a** interstitial fluid pressure; **b** principal shear stress; **c** fluid pressure load support; where, *Model 1* patient-specific collagen fiber network, inhomogeneous compositional parameters; *Model 2* patient-specific collagen fiber network, homogeneous compositional parameters; *Model 3* no collagen fiber network, inhomogeneous compositional parameters; *Model 4* no collagen fiber network, homogeneous compositional parameters

Reviewing quantitative values in the simulation results, the maximum interstitial fluid pressure at the indentation surface is 11.0 kPa for Model 1 (maximum among models); 10.1 kPa for Model 2 (a drop of  $-8.18\%$  relative to Model 1); 4.10 kPa for Model 3 ( $-62.7\%$  relative to Model 1); and 3.46 kPa for Model 4 ( $-68.5\%$  relative to Model 1). Reviewing the principal shear stress similarly, the maximum intra-tissue value is 8.64 kPa for Model 2 (maximum among models); 8.41 kPa for Model 1 (a drop

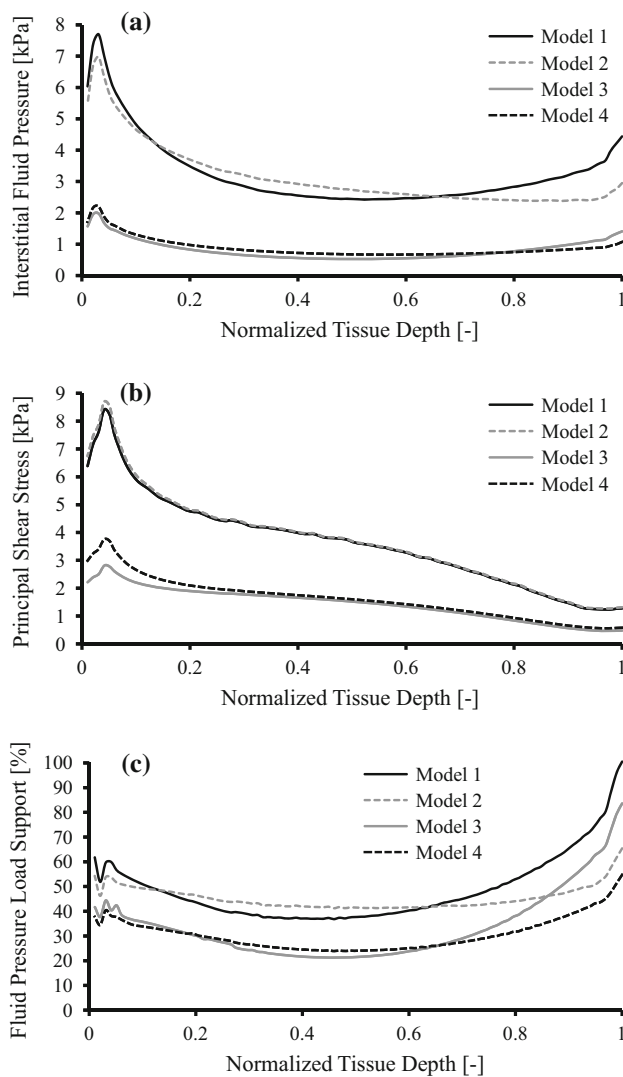


**Fig. 5** Simulation results plotted along the *dashed line* in Fig. 2b, i.e., through the tissue thickness at the edge of the indenter, for the indentation experiment with an impermeable, plane-ended cylinder of diameter 1 mm compressing the cartilage sample to 1% global strain in 150 s: **a** interstitial fluid pressure; **b** principal shear stress; **c** fluid pressure load support; where, *Model 1* patient-specific collagen fiber network, inhomogeneous compositional parameters; *Model 2* patient-specific collagen fiber network, homogeneous compositional parameters; *Model 3* no collagen fiber network, inhomogeneous compositional parameters; *Model 4* no collagen fiber network, homogeneous compositional parameters

of  $-2.66\%$  relative to Model 2); 2.78 kPa for Model 3: ( $-67.8\%$  relative to Model 2); and 3.68 kPa for Model 4 ( $-57.4\%$  relative to Model 2).

## 5 Discussion

We propose a new 3D finite strain model capable of simultaneously addressing both solid (reinforcement) and fluid (per-

meability) dependence of the tissue's mechanical response on the patient-specific collagen fiber network. We represent fiber reinforcement as an inhomogeneous, dispersed network, where the fluid permeability is intimately dependent on this network and on a fixed intrafibrillar water portion. Our approach, in which the model parameters are physically motivated, implements image-based morphological data in a computational setting. We demonstrate the modeling approach by retesting two hypotheses from the cartilage mechanics literature on a specific sample of cartilage. Following our previous work (Pierce et al. 2013b), we select indentation to 1% global strain in 150 s because it allows some time for loss of fluid pressure (for testing the two hypotheses) while still being in the early time response relevant from a physiologic perspective (mechanical equilibrium generally occurs on a timescale of thousands of seconds) (Ateshian et al. 1997; Pierce et al. 2009).

Discussing the results specifically, Figs. 3a, c, e, g, 4a and 5a compare the interstitial fluid pressure distributions under the indenter predicted by the four models. Figures 4a and 5a compare this through the thickness of the tissue both along the main axis of the indenter and at the edge of the indenter—i.e., along the dashed line in Fig. 2b—respectively. In our numerical solution for the distribution of pressure, we set the filtration velocity to zero in the directions normal to impermeable surfaces. This solution should give us  $\text{grad } p$ , normal to these surfaces, which is numerically zero [cf. (16) in the absence of significant body forces]. In practice, the solution may not give exactly  $\text{grad } p$  equals zero, normal to these surfaces, because we evaluate the equations at Gauss quadrature points and project this solution to the nodes. Nonetheless, the main gradient in pressure is parallel to the impermeable surfaces within the limitations of the FE method (cf., e.g., Fig. 3a). Overall, Model 1 retains the highest interstitial fluid pressure among the four models, and the fluid pressure is concentrated in the superficial zone and particularly the articular surface. Not surprisingly, the fluid pressure is higher directly underneath the edge of the indenter versus underneath its center. Otherwise, Figs. 4a and 5a show similar trends in fluid pressure versus normalized tissue depth. The result for Model 1, in the context of the full results, demonstrates that both the fiber network and the tissue's inhomogeneity modulate the fluid pressure distribution to maintain fluid pressure beneath the contact surface and thus enhance load support and surface frictional properties. Model 2 demonstrates a similar fluid pressure profile, although at a slightly lower ( $\approx -8\%$ ) pressure at the articular surface and a significantly lower pressure near the subchondral bone. Models 3 and 4 show dramatic drops in interstitial fluid pressure ( $\approx -63$  and  $\approx -69\%$ , respectively), and nearly identical fluid pressure profiles with the pressure relatively constant throughout the thickness of the tissue.

Column 2 of Figs. 3b, d, f, h, 4b and 5b compare the principal (maximum) shear stress distributions in the tissue solid predicted by the four models. Inappropriate mechanical loading of the joint causes cartilage degradation, and studies implicate shear forces as a critical component in the destructive cycle (Smith et al. 2000). We study the principal shear stress in the solid because destructive effects are known to be associated with shear stress in particular (Smith et al. 2000, 2004; Wang et al. 2010a, b; Zhu et al. 2010; Bader et al. 2011). The principal shear stress distributions through the tissue thickness for both Models 3 and 4 are significantly lower ( $\approx 60\%$  reduction in peak values) relative to Models 1 and 2, which are similar. Thus, collagen network reinforcement significantly increases the shear stress in the cartilage tissue. This is likely due to the fact that we apply the same fixed global strain to all models, although the relative stiffness of the materials differs. Hence, it will take larger forces to compress Models 1 and 2 versus Models 3 and 4, thus leading to higher stresses. Generalizing, the solid extra stress results between fiber network-reinforced and unreinforced models should be viewed with caution as the fiber-reinforced material is relatively stiffer. Interestingly, Models 1 and 2 show the highest shear stress in the middle zone along the main axis of the indenter, cf. Fig. 4b. Clark and Simonian (1997) hypothesize that (1) the earliest change in the collagen matrix structure is loosening of the cross-links between large fibrils (which themselves remain intact initially), and that (2) this interfibrillar loosening mechanism initiates in the middle zone of cartilage rather than at the surface. During later stages of degeneration, the collagen fiber network becomes less organized, disrupting even the solid matrix and finally effecting the gross cartilage volume. Finally, Models 1 and 2 show an  $\approx 3\%$  difference in peak shear stress near the articular surface underneath the edge of the indenter, cf. Fig. 5b. These results may indicate that inhomogeneity in the material parameters through the thickness of the cartilage serves to reduce the detrimental effects of intra-tissue shear stress.

Figures 4c and 5c compare the fluid pressure load support distributions under the indenter predicted by the four models. Overall, the models including the fiber network (Models 1 and 2) generally have better fluid pressure load support. While Model 1 has the highest interstitial fluid pressure, the fluid pressure load support in the superficial zones of Models 1 and 2 is similar, while this is lower in Models 3 and 4. Surprisingly, the trend in the deep zones is different. Here the fluid pressure load support of Models 1 and 3 is similar, and this is lower in Models 2 and 4. These results may indicate that the collagen fiber network may serve to increase fluid pressure load support near the articular surface, while inhomogeneity in the material parameters in the deep zone may serve to increase fluid pressure load support near the subchondral bone.

Overall, the results of this study support both hypotheses. For the tissue sample investigated, the through-the-thickness inhomogeneity of both the collagen fiber network and of the material parameters serve to influence the interstitial fluid pressure distribution and maintain fluid pressure near the cartilage surface. More specifically, our results demonstrate that the fiber network dramatically increases interstitial fluid pressure, and focuses it near the surface. This is important because increased fluid pressure at the articular surface reduces the coefficient of friction of the interface, thus improving motion and reducing wear (Ateashian et al. 1998). Furthermore, inhomogeneity in the material parameters increases fluid pressure and reduces principal shear stress in the solid. According to these results, inhomogeneity in the orientation of the fiber network through the thickness of the cartilage appears to have a larger effect than inhomogeneity of the material parameters on this cartilage sample's advantageous distribution of interstitial fluid pressure in response to mechanical loading. Additionally, a biphasic neo-Hookean material model, as is available in commercial FE codes such as ABAQUS, does not capture important features of the tissue response: e.g., distributions of interstitial fluid pressure and principal shear stress.

In our previous study, Pierce et al. (2013b), our results supported both hypotheses, but we concluded that inhomogeneity in the material parameters (vs. the collagen fiber network) through the thickness appeared to have a larger effect on fluid pressure retention and distribution in this tissue sample. Conversely, the results of our current study indicate that of the two sources of inhomogeneity probed, inhomogeneity in the orientation of the fiber network through the thickness of the cartilage appears to have the larger effect on the tissue's advantageous distribution of fluid pressure. We attribute the difference in outcomes to three improvements in the fidelity of the constitutive model. First, we improved the representation of collagen network in two ways: (1) a more accurate implementation of DT-MRI data and hence likely a better representation of the local collagen network throughout the tissue; (2) an improved formulation for the mechanical response of the fibers themselves, whereby only fibers truly in tension contribute to the total strain energy. Second, we improved the representation of inhomogeneity in the model parameters where these are now continuous through the thickness. In the previous work this inhomogeneity was represented as piece-wise constant (homogeneous within each of the three tissue zones) which likely contributed to the sharp kinks (curves which are not  $C^1$  continuous) in the through-the-thickness distributions of the responses investigated, cf. Fig. 3c, d in Pierce et al. (2013b). Third, we extended the model to include viscous effects in both the proteoglycan and collagen solids as has been demonstrated experimentally, cf. Huang et al. (2001).

Naturally, there are a number of limitations and areas for future improvements in the proposed material model. We assume constant electrolytic conditions and lump the Donnan osmotic pressure with the stiffness of the solid matrix. Thus, the model cannot capture the effects of osmotic swelling, cf. [Chahine et al. \(2004\)](#), [Ateshian et al. \(2004\)](#) and references therein, which may induce prestraining of the collagen fibers. Additionally, the representation of the fiber network does not include fiber–fiber or matrix–fiber interactions, or the effects of fibrillar cross-links.

While we have improved the representation of inhomogeneity in the model parameters such that they vary continuously through the thickness (cf. [Krishnan et al. 2003](#)), we have still employed ‘generic’ properties taken from the cartilage mechanics literature and our prior work ([Pierce et al. 2013a, b](#)). Future experimental work should be aimed at determining improved material parameters including their mean and standard deviation for inter- and intra-patient variability. We also hope to extract even more sample-specific information from diffusion-weighted images. In particular, it appears likely that the Darcy hydraulic permeability  $k_{0S}(z^*)$  can be estimated directly from DT-MRI data, cf. [Sarntinorant et al. \(2006\)](#) and [Fernandez et al. \(2014\)](#).

We use state-of-the-art DT-MRI measurement techniques to infer both geometric as well as structural properties of the sample tested. However, a number of limitations in the DT-MRI impair the model’s fidelity. Among these limitations, the so-called partial volume effect has by far the biggest impact ([Alexander et al. 2001](#)). In fitting the data to determine the local diffusion tensors, we violate everywhere the assumption of homogeneous diffusion properties within a single measurement voxel ( $50 \times 100 \times 800 \mu\text{m}$ ), and particularly along the sample’s interface with the fluid bath and at the cartilage–bone transition. As outlined by [Alexander et al. \(2001\)](#), averaging inhomogeneous responses within a single compartment can decrease the observed anisotropy, i.e., the collagen fibers appear to be more uniformly distributed than they are in reality. The most obvious solution to this problem—reducing the voxel size—would lead either to a lower signal-to-noise ratio or to an increased measurement time. Alternatively, we could apply more complex diffusion models to capture multiple fiber directions within a single measurement voxel. [Tuch \(2004\)](#), e.g., proposed a model based on spherical radial basis functions which can resolve fibers crossing, bending or twisting within an individual voxel. The downside of such models is that they require a large number of diffusion-weighted images to constrain all of the degrees of freedom, which in turn leads to increased measurement times.

In conclusion, high-fidelity, intra-tissue simulations allow us to consider complex problems in structure–function relationships, load support, contact and loading effects on cartilage degeneration, and provide insight to the mechanobi-

ological cellular stimuli. Furthermore, 3D FE modeling of cartilage, calibrated using medical imaging modalities, has potential to become a clinical diagnostic tool for patient-specific analysis in the future.

**Acknowledgments** We thank Lukas Moj from the TU Dortmund University, for help with element programming; Thomas S.E. Eriksson from the University of Oxford, for help with ParFEAP; José Raya and Christian Glaser from the NYU Langone Medical Center for use of the diffusion tensor magnetic resonance imaging data; and Magnus B. Lilledahl from the Norwegian University of Science and Technology for generously providing us with the multi-photon microscopy image (Fig. 1, left).

### Appendix 1

To evaluate integrals over the unit sphere, as shown, e.g., in (8) and (10), we apply the numerical method suggested by [Bažant and Oh \(1986\)](#) using  $m$  distinct direction vectors  $\mathbf{M}^i$ ,  $i = 1, 2, \dots, m$ . Symmetry of our method allows us to use only half the number of direction vectors, and subsequently double the integration weights  $q^i$ . With this approach we numerically estimate integrals as

$$\int_{\Omega} A(\mathbf{M})d\Omega = \int_{\theta=0}^{2\pi} \int_{\phi=0}^{\pi} A(\theta, \phi) \sin \theta \, d\phi d\theta \tag{19}$$

$$\approx 4\pi \sum_{i=1}^m A(\mathbf{M}^i)2q^i,$$

where  $A$  is a function taking tensor arguments. A table of the direction vectors and associated integration weights can be found in Table 1 of [Bažant and Oh \(1986\)](#).

### Appendix 2

To obtain solutions of nonlinear problems in computational finite (visco)elasticity via incremental solution techniques of Newton’s type, we solve a series of linearized problems and thus require the linearized constitutive equations. Specifically, we require elasticity tensors for both the isotropic matrix and fiber network contributions to the solid extra stress, as well as the derivative of the filtration velocity  $n^F \mathbf{w}_{FS}$  with respect to both the deformation gradient  $\mathbf{F}_S$  and the material gradient of the interstitial fluid pressure  $\text{grad } p$ . We write the filtration velocity in the current configuration as (16) and (17) [cf. [Pierce et al. \(2013a, 2013b\)](#)]. In the reference configuration, we write the filtration velocity  $n^F \mathbf{w}_{FS0}$  as

$$n^F \mathbf{w}_{FS0} = k_{0S} \left( \frac{n^F}{1 - n_{0S}^S} \right)^m \times \mathbf{H}_0 \left( -J_S \text{grad } p + J_S \rho^{\text{FR}} \mathbf{F}_S^T \mathbf{b} \right), \tag{20}$$

with,

$$\mathbf{H}_0 = \frac{1}{4\pi} \int_{\Omega} \frac{\rho(\mathbf{M})}{I_4(\mathbf{M})} \mathbf{M} \otimes \mathbf{M} \, d\Omega. \tag{21}$$

We write the derivative of the filtration velocity in the reference configuration with respect to the deformation gradient of the solid, i.e.,  $\partial(n^F \mathbf{w}_{FS0})/\partial \mathbf{F}_S$ , as

$$\begin{aligned} \partial(n^F \mathbf{w}_{FS0})/\partial \mathbf{F}_S &= \partial/\partial \mathbf{F}_S \left[ k_{0S} \left( \frac{n^F}{1 - n_{0S}^S} \right)^m \right. \\ &\quad \left. \mathbf{H}_0 \left( -J_S \text{grad } p + J_S \rho^{FR} \mathbf{F}_S^T \mathbf{b} \right) \right] \\ &= k_{0S} \left( \frac{n^F}{1 - n_{0S}^S} \right)^m \left[ -\frac{\partial \mathbf{H}_0}{\partial \mathbf{F}_S} J_S \text{grad } p \right. \\ &\quad - \mathbf{H}_0 \otimes \frac{\partial J_S}{\partial \mathbf{F}_S} \text{grad } p + \rho^{FR} \frac{\partial \mathbf{H}_0}{\partial \mathbf{F}_S} J_S \mathbf{F}_S^T \mathbf{b} \\ &\quad \left. + \rho^{FR} \mathbf{H}_0 \frac{\partial J_S}{\partial \mathbf{F}_S} \otimes \mathbf{F}_S^T \mathbf{b} + \rho^{FR} \mathbf{H}_0 J_S \frac{\partial \mathbf{F}_S^T}{\partial \mathbf{F}_S} \mathbf{b} \right], \tag{22} \end{aligned}$$

with,

$$\begin{aligned} \partial \mathbf{H}_0/\partial \mathbf{F}_S &= \partial/\partial \mathbf{F}_S \left[ \frac{1}{4\pi} \int_{\Omega} \frac{\rho(\mathbf{M})}{I_4(\mathbf{M})} \mathbf{M} \otimes \mathbf{M} \, d\Omega \right] \\ &= \frac{1}{4\pi} \int_{\Omega} \rho(\mathbf{M}) \frac{\partial I_4(\mathbf{M})^{-1}}{\partial \mathbf{F}_S} \otimes \mathbf{M} \otimes \mathbf{M} \, d\Omega, \tag{23} \end{aligned}$$

and

$$\begin{aligned} \partial I_4(\mathbf{M})^{-1}/\partial \mathbf{F}_S &= \frac{\partial I_4(\mathbf{M})^{-1}}{\partial I_4(\mathbf{M})} \frac{\partial I_4(\mathbf{M})}{\partial \mathbf{C}_S} : \frac{\partial \mathbf{C}_S}{\partial \mathbf{F}_S} \\ &= -I_4(\mathbf{M})^{-2} \mathbf{M} \otimes \mathbf{M} : \left( \frac{\partial \mathbf{F}_S^T}{\partial \mathbf{F}_S} \mathbf{F}_S \right. \\ &\quad \left. + \mathbf{F}_S^T \frac{\partial \mathbf{F}_S}{\partial \mathbf{F}_S} \right). \tag{24} \end{aligned}$$

In index notation, we write the results from (22)<sub>2</sub>–(24)<sub>2</sub> as

$$\begin{aligned} (\partial(n^F \mathbf{w}_{FS0})/\partial \mathbf{F}_S)_{IJK} &= k_{0S} \left( \frac{n^F}{1 - n_{0S}^S} \right)^m \\ &\quad \times \left[ -\left( \frac{\partial \mathbf{H}_0}{\partial \mathbf{F}_S} \right)_{IJKL} J_S (\text{grad } p)_L \right. \\ &\quad - (\mathbf{H}_0)_{IJ} \left( \frac{\partial J_S}{\partial \mathbf{F}_S} \right)_{KL} (\text{grad } p)_L \\ &\quad + \rho^{FR} \left( \frac{\partial \mathbf{H}_0}{\partial \mathbf{F}_S} \right)_{IJKM} J_S (\mathbf{F}_S^T)_{ML} (\mathbf{b})_L \\ &\quad \left. + \rho^{FR} (\mathbf{H}_0)_{IM} \left( \frac{\partial J_S}{\partial \mathbf{F}_S} \right)_{MJ} (\mathbf{F}_S^T)_{KL} (\mathbf{b})_L \right] \end{aligned}$$

$$+ \rho^{FR} (\mathbf{H}_0)_{IM} J_S \left( \frac{\partial \mathbf{F}_S^T}{\partial \mathbf{F}_S} \right)_{MJKL} (\mathbf{b})_L \tag{25}$$

where  $(\partial \mathbf{F}_S^T/\partial \mathbf{F}_S)_{IJKL} = \delta_{JK} \delta_{IL}$ , with  $\delta_{IJ} = \mathbf{e}_I \cdot \mathbf{e}_J$  the Kronecker delta, and with

$$\begin{aligned} (\partial \mathbf{H}_0/\partial \mathbf{F}_S)_{IJKL} &= \frac{1}{4\pi} \int_{\Omega} \rho(\mathbf{M}) \left( \frac{\partial I_4(\mathbf{M})^{-1}}{\partial \mathbf{F}_S} \right)_{IJ} (\mathbf{M} \otimes \mathbf{M})_{KL} \, d\Omega, \tag{26} \end{aligned}$$

and

$$\begin{aligned} \left( \frac{\partial I_4(\mathbf{M})^{-1}}{\partial \mathbf{F}_S} \right)_{IJ} &= -I_4(\mathbf{M})^{-2} (\mathbf{M} \otimes \mathbf{M})_{KL} [\delta_{KJ} (\mathbf{F}_S)_{IL} + (\mathbf{F}_S)_{IK} \delta_{LJ}]. \tag{27} \end{aligned}$$

To continue, we write the derivative of the filtration velocity in the reference configuration with respect to the material gradient of the interstitial fluid pressure, i.e.,  $\partial(n^F \mathbf{w}_{FS0})/\partial \text{grad } p$ , as

$$\begin{aligned} \partial(n^F \mathbf{w}_{FS0})/\partial \text{grad } p &= -k_{0S} \left( \frac{n^F}{1 - n_{0S}^S} \right)^m \mathbf{H}_0 J_S \frac{\partial \text{grad } p}{\partial \text{grad } p}. \tag{28} \end{aligned}$$

In index notation, we write (28) as

$$\begin{aligned} \left( \partial(n^F \mathbf{w}_{FS0})/\partial \text{grad } p \right)_{IJ} &= -k_{0S} \left( \frac{n^F}{1 - n_{0S}^S} \right)^m J_S (\mathbf{H}_0)_{IK} \delta_{KJ}. \tag{29} \end{aligned}$$

### Appendix 3

In a ‘classic’ DT-MRI experiment, the tensor data is reconstructed from six or more diffusion-weighted images under the modeling assumption of a single Gaussian diffusion compartment per voxel (Tuch 2004). In Cartesian coordinates the anisotropic Gaussian probability distribution function (PDF) for a single voxel can be stated according to (1), where therein  $(\boldsymbol{\xi}) = (x, y, z)^T$  denotes the relative displacement of water molecules. Since we are only interested in the orientation density function (ODF) we drop the diffusion time by setting  $\delta = 0.5 \text{ s}$  and, without loss of generality, drop the  $b$ -value by setting  $b = 1.0 \text{ s/mm}^2$ , yielding the familiar form of the multivariate normal distribution (with zero mean)

$$P(\boldsymbol{\xi}) = (2\pi)^{-3/2} |\mathbf{D}|^{-1/2} \exp \left\{ -\frac{1}{2} \boldsymbol{\xi}^T \mathbf{D}^{-1} \boldsymbol{\xi} \right\}. \tag{30}$$

Due to the simple analytic form of the diffusion probability density, a closed form ODF can be computed. We first convert (30) to spherical coordinates

$$x = r \cos \theta \sin \phi, \quad y = r \sin \theta \sin \phi, \quad z = r \cos \phi, \quad (31)$$

with  $r \in [0, \infty)$ ,  $\theta \in [0, 2\pi)$ , and  $\phi \in [0, \pi]$ . Next, we marginalize out the radius  $r$ , account for the factor of  $4\pi$  in (8) and the required ODF results as

$$\rho(\mathbf{M}, \mathbf{D}) = \left(\frac{2}{\pi}\right)^{1/2} |\mathbf{D}|^{-1/2} \times \int_0^\infty \exp\left\{-\frac{1}{2}r^2\mathbf{M}^T\mathbf{D}^{-1}\mathbf{M}\right\} r^2 \sin \theta \, dr, \quad (32)$$

which gives (18). Note that the Jacobian determinant  $r^2 \sin \theta$  is introduced by the change from Cartesian to spherical coordinates to account for the fact that the surface element on the sphere is not uniform across the entire domain. Assuming the symmetric, positive-definite diffusion tensor is given as

$$(\mathbf{D}) = \begin{pmatrix} D_{xx} & D_{xy} & D_{xz} \\ D_{xy} & D_{yy} & D_{yz} \\ D_{xz} & D_{yz} & D_{zz} \end{pmatrix}, \quad (33)$$

the ODF can be written as

$$\begin{aligned} \rho(\mathbf{M}, \mathbf{D}) = \sin \theta / & \left\{ \left( - \left( D_{xz}^2 D_{yy} \right) + 2D_{xy} D_{xz} D_{yz} \right. \right. \\ & \left. \left. - D_{xx} D_{yz}^2 - D_{xy}^2 D_{zz} + D_{xx} D_{yy} D_{zz} \right)^{1/2} \right. \\ & \left( \left( \left( D_{xy}^2 - D_{xx} D_{yy} \right) \cos^2 \phi \right. \right. \\ & \left. \left. + \left( D_{yz}^2 - D_{yy} D_{zz} \right) \cos^2 \theta \sin^2 \phi \right. \right. \\ & \left. - D_{xy} D_{xz} \sin 2\phi \sin \theta + D_{xx} D_{yz} \sin 2\phi \sin \theta \right. \\ & \left. + D_{xz}^2 \sin^2 \phi \sin^2 \theta - D_{xx} D_{zz} \sin^2 \phi \sin^2 \theta \right. \\ & \left. + \cos \theta \left[ \left( D_{xz} D_{yy} - D_{xy} D_{yz} \right) \sin 2\phi \right. \right. \\ & \left. \left. - 2D_{xz} D_{yz} \sin^2 \phi \sin \theta \right] \right. \\ & \left. + D_{xy} D_{zz} \sin^2 \phi \sin 2\theta \right) \\ & / \left[ \left( D_{xz}^2 D_{yy} - 2D_{xy} D_{xz} D_{yz} + D_{xy}^2 D_{zz} \right. \right. \\ & \left. \left. + D_{xx} \left( D_{yz}^2 - D_{yy} D_{zz} \right) \right)^{2/3} \right] \}. \end{aligned}$$

Note that most trigonometric functions and several sub-expressions could be pre-computed within a FE implementation, in particular when a numerical integration scheme is used and only certain directions are evaluated.

## References

Abdullah OM, Othman SF, Zhou XJ, Magin RL (2007) Diffusion tensor imaging as an early marker for osteoarthritis. In: Proceedings of the international society for magnetic resonance in medicine 2007, p 814

- Alexander AL, Hasan KM, Lazar M, Tsuruda JS, Parker DL (2001) Analysis of partial volume effects in diffusion-tensor MRI. *Magn Reson Med* 45:770–780
- Arsigny V, Fillard P, Pennec X, Ayache N (2006) Geometric means in a novel vector space structure on symmetric positive-definite matrices. *SIAM J Matrix Anal Appl* 29:328–347
- Ateshian GA, Chahine NO, Basalo IM, Hung CT (2004) The correspondence between equilibrium biphasic and triphasic material properties in mixture models of articular cartilage. *J Biomech* 37:391–400
- Ateshian GA, Rajan V, Chahine NO, Canal CE, Hung CT (2009) Modeling the matrix of articular cartilage using a continuous fiber angular distribution predicts many observed phenomena. *J Biomech Eng* 131:61003
- Ateshian GA, Wang H, Lai WM (1998) The role of interstitial fluid pressurization and surface porosities on the boundary friction of articular cartilage. *J Tribol ASME* 120:241–251
- Ateshian GA, Warden WH, Kim JJ, Grelsamer RP, Mow VC (1997) Finite deformation biphasic material properties of bovine articular cartilage from confined compression experiments. *J Biomech* 30:1157–1164
- Athanasios KA, Darling EM, Hu JC (eds) (2010) Articular cartilage tissue engineering. Morgan & Claypool, San Rafael
- Bachrach NM, Mow VC, Guilak F (1998) Incompressibility of the solid matrix of articular cartilage under high hydrostatic pressures. *J Biomech* 31:445–451
- Bader DL, Salter DM, Chowdhury TT (2011) Biomechanical influence of cartilage homeostasis in health and disease. *Arthritis* 2011. doi:10.1155/2011/979032
- Bae WC, Lewis CW, Levenston ME, Sah RL (2006) Indentation testing of human articular cartilage: effects of probe tip geometry and indentation depth on intra-tissue strain. *J Biomech* 39:1039–1047
- Basser PJ, Mattiello J, LeBihan D (1994) MR diffusion tensor spectroscopy and imaging. *Biophys J* 66:259–267
- Basser PJ, Schneiderman R, Bank RA, Wachtel E, Maroudas A (1998) Mechanical properties of the collagen network in human articular cartilage as measured by osmotic stress technique. *Arch Biochem Biophys* 351:207–219
- Bažant ZP, Oh BH (1986) Efficient numerical integration on the surface of a sphere. *Z Angew Math Mech* 66:37–49
- Bishop AW (1959) The principle of effective stress. *Tek Ukeblad* 39:859–863
- Bluhm J (2002) Modelling of saturated thermo-elastic porous solids with different phase temperatures. In: Ehlers W, Bluhm J (eds) Porous media: theory, experiments and numerical applications. Springer, Berlin, pp 87–120
- Bowen RM (1980) Incompressible porous media models by use of the theory of mixtures. *Int J Eng Sci* 18:1129–1148
- Bowen RM (1982) Compressible porous media models by use of the theory of mixtures. *Int J Eng Sci* 20:697–735
- Chahine NO, Wang CC, Hung CT, Ateshian GA (2004) Anisotropic strain-dependent material properties of bovine articular cartilage in the transitional range from tension to compression. *J Biomech* 37:1251–1261
- Charlebois M, McKee MD, Buschmann MD (2004) Nonlinear tensile properties of bovine articular cartilage and their variation with age and depth. *J Biomech Eng* 126:129–137
- Chen AC, Bae WC, Schinagl RM, Sah RL (2001) Depth- and strain-dependent mechanical and electromechanical properties of full-thickness bovine articular cartilage in confined compression. *J Biomech* 34:1–12
- Clark JM, Simonian PT (1997) Scanning electron microscopy of “fibrillated” and “malacic” human articular cartilage: technical considerations. *Microsc Res Tech* 37:299–313
- de Boer R (2000) Theory of porous media. Highlights in the historical development and current state. Springer, Heidelberg

- de Visser SK, Crawford RW, Pope JM (2008a) Structural adaptations in compressed articular cartilage measured by diffusion tensor imaging. *Osteoarthr Cartil* 16:83–89
- de Visser SK, Bowden JC, Wentrup-Bryne E, Rintoul L, Bostrom T, Pope JM, Momot KI (2008b) Anisotropy of collagen fibre alignment in bovine cartilage: comparison of polarised light microscopy and spatially resolved diffusion-tensor measurements. *Osteoarthr Cartil* 16:689–697
- DiSilvestro MR, Suh JKF (2001) A cross-validation of the biphasic poroviscoelastic model of articular cartilage in unconfined compression, indentation, and confined compression. *J Biomech* 34:519–525
- Ehlers W (1989) Poröse Medien—ein kontinuumsmechanisches Modell auf der Basis der Mischungstheorie. Ph.D. thesis. Universität GH Essen. Forschungsbericht aus dem Fachbereich Bauwesen 47
- Ehlers W (1993) Constitutive equations for granular materials in geomechanical context. In: Hutter K (ed) *Continuum mechanics in environmental sciences and geophysics*. Springer, Wien, pp 313–402. CISM Courses and Lectures no. 337
- Ehlers W (2002) Foundations of multiphase and porous materials. In: Ehlers W, Bluhm J (eds) *Porous media: theory. Experiments and numerical applications*, Springer, Berlin, pp 3–86
- Eipper G (1998) Theorie und Numerik finiter elastischer Deformationen in fluidgesättigten porösen Festkörpern. Ph.D. thesis. Universität Stuttgart. Bericht Nr. II-1 aus dem Institut für Mechanik (Bauwesen)
- Federico S, Gasser TC (2010) Nonlinear elasticity of biological tissues with statistical fibre orientation. *J R Soc Interface* 7:955–966
- Federico S, Grillo A (2012) Elasticity and permeability of porous fibre reinforced materials under large deformations. *Mech Mater* 44:58–71
- Federico S, Herzog W (2008) On the anisotropy and inhomogeneity of permeability in articular cartilage. *Biomech Model Mechanobiol* 7:367–378
- Fernandez M, Jambawalikar S, Myers K (2014) Toward quantitative biomarkers of cervical structural health: development of mri tools for in-vivo mechanical property measurement. In: *Proceedings of the international society for magnetic resonance in medicine*, p 2217
- Filidoro L, Dietrich O, Weber J, Rauch E, Oether T, Wick M, Reiser MF, Glaser C (2005) High-resolution diffusion tensor imaging of human patellar cartilage: feasibility and preliminary findings. *Magn Reson Med* 53:993–998
- García JJ, Cortés DH (2007) A biphasic viscohyperelastic fibril-reinforced model for articular cartilage: formulation and comparison with experimental data. *J Biomech* 40:1737–1744
- Gasser TC, Ogden RW, Holzapfel GA (2006) Hyperelastic modelling of arterial layers with distributed collagen fibre orientations. *J R Soc Interface* 3:15–35
- Hascall VC (1977) Interaction of cartilage proteoglycans with hyaluronic acid. *J Supramol Struct* 7:101–120
- Herrmann LR, Peterson FE (1968) A numerical procedure for viscoelastic stress analysis. In: *Proceedings 7th meeting of ICRPG mechanical behavior working group*, Orlando
- Holzapfel GA (1996) On large strain viscoelasticity: continuum formulation and finite element applications to elastomeric structures. *Int J Numer Methods Eng* 39:3903–3926
- Holzapfel GA, Gasser TC (2001) A viscoelastic model for fiber-reinforced composites at finite strains: continuum basis, computational aspects and applications. *Comput Methods Appl Mech Eng* 190:4379–4403
- Holzapfel GA, Gasser TC, Ogden RW (2000) A new constitutive framework for arterial wall mechanics and a comparative study of material models. *J Elast* 61:1–48
- Holzapfel GA, Unterberger MJ, Ogden RW (2014) An affine continuum mechanical model for cross-linked F-actin networks with compliant linker proteins. *J Mech Behav Biomed Mater* 38:78–90
- Huang CY, Mow VC, Ateshian GA (2001) The role of flow-independent viscoelasticity in the biphasic tensile and compressive responses of articular cartilage. *J Biomech Eng* 123:410–417
- Huang CY, Stankiewicz A, Ateshian GA, Mow VC (2005) Anisotropy, inhomogeneity, and tension-compression nonlinearity of human glenohumeral cartilage in finite deformation. *J Biomech* 38:799–809
- Humphrey JD (2002) *Cardiovascular solid mechanics. Cells, tissues, and organs*. Springer, New York
- Jurvelin JS, Buschmann MD, Hunziker EB (1997) Optical and mechanical determination of Poisson's ratio of adult bovine humeral articular cartilage. *J Biomech* 30:235–241
- Krishnan R, Park S, Echststein F, Ateshian GA (2003) Inhomogeneous cartilage properties enhance superficial interstitial fluid support and frictional properties, but do not provide a homogeneous state of stress. *J Biomech Eng* 125:569–577
- Lei F, Szeri AZ (2006) The influence of fibril organization on the mechanical behaviour of articular cartilage. *Proc R Soc Lond A* 462:3301–3322
- Li LP, Herzog W (2004) The role of viscoelasticity of collagen fibers in articular cartilage: theory and numerical formulation. *Biorheology* 41:181–194
- Maas SA, Ellis BJ, Ateshian GA, Weiss JA (2012) FEBio: finite elements for biomechanics. *J Biomech Eng* 134:011005
- Meder R, de Visser SK, Bowden JC, Bostrom T, Pope JM (2006) Diffusion tensor imaging of articular cartilage as a measure of tissue microstructure. *Osteoarthr Cartil* 14:875–881
- Miehe C, Göktepe S (2005) A micromacro approach to rubber-like materials—part II: the micro-sphere model of finite rubber viscoelasticity. *J Mech Phys Solids* 53:2231–2258
- Miehe C, Göktepe S, Lulei F (2004) A micro-macro approach to rubber-like materials—part I: the non-affine micro-sphere model of rubber elasticity. *J Mech Phys Solids* 52:2617–2660
- Mow VC, Gu WY, Chen FH (2005) Structure and function of articular cartilage and meniscus. In: Mow VC, Huiskes R (eds) *Basic orthopaedic biomechanics & mechano-biology*, 3rd edn. Lippincott Williams & Wilkins, Philadelphia, pp 181–258
- Muir H (1983) Proteoglycans as organizers of the intercellular matrix. *Biochem Soc Trans* 11:613–622
- Park S, Krishnan R, Nicoll SB, Ateshian GA (2003) Cartilage interstitial fluid load support in unconfined compression. *J Biomech* 36:1785–1796
- Pence TJ (2012) On the formulation of boundary value problems with the incompressible constituents constraint in finite deformation poroelasticity. *Math Methods Appl Sci* 35:1756–1783
- Pierce DM, Ricken T, Holzapfel GA (2013a) A hyperelastic biphasic fiber-reinforced model of articular cartilage considering distributed collagen fiber orientations: continuum basis, computational aspects and applications. *Comput Methods Biomech Biomed Eng* 16:1344–1361
- Pierce DM, Ricken T, Holzapfel GA (2013b) Modeling sample/patient-specific structural and diffusional response of cartilage using DT-MRI. *Int J Numer Methods Biomed Eng* 29:807–821
- Pierce DM, Trobin W, Raya JG, Trattnig S, Bischof H, Glaser C, Holzapfel GA (2010) DT-MRI based computation of collagen fiber deformation in human articular cartilage: a feasibility study. *Ann Biomed Eng* 38:2447–2463
- Pierce DM, Trobin W, Trattnig S, Bischof H, Holzapfel GA (2009) A phenomenological approach toward patient-specific computational modeling of articular cartilage including collagen fiber tracking. *J Biomech Eng* 131:091006

- Price WS (2009) NMR studies of translational motion: principles and applications. Cambridge University Press, Cambridge
- Raya JG, Melkus G, Adam-Neumair S, Dietrich O, Mützel E, Kahr B, Reiser MF, Jakob PM, Putz R, Glaser C (2011) Change of diffusion tensor imaging parameters in articular cartilage with progressive proteoglycan extraction. *INVRAD* 46:401–409
- Raya JG, Melkus G, Adam-Neumair S, Dietrich O, Mützel E, Reiser MF, Putz R, Kirsch T, Jakob PM, Glaser C (2013) Diffusion-tensor imaging of human articular cartilage specimens with early signs of cartilage damage. *RADIO* 266:831–841
- Ricken T, Bluhm J (2010) Remodeling and growth of living tissue: a multiphase theory. *Arch Appl Mech* 80:453–465
- Sáez P, Alastrué V, Peña E, Doblaré M, Martínez M (2012) Anisotropic microsphere-based approach to damage in soft fibered tissue. *Biomech Model Mechanobiol* 11:595–608
- Santinoranont M, Chen X, Zhao J, Mareci TH (2006) Computational model of interstitial transport in the spinal cord using diffusion tensor imaging. *Ann Biomed Eng* 34:1304–1321
- Simo JC (1987) On a fully three-dimensional finite-strain viscoelastic damage model: formulation and computational aspects. *Comput Methods Appl Mech Eng* 60:153–173
- Simo JC, Pister KS (1984) Remarks on rate constitutive equations for finite deformation problems: computational implications. *Comput Methods Appl Mech Eng* 46:201–215
- Skempton AW (1960) Terzaghi's discovery of effective stress. In: Bjerrum L, Casagrande A, Peck RB, Skempton AW (eds) *From theory to practice in soil mechanics*. Wiley, New York, pp 42–53
- Smith RL, Carter DR, Schurman DJ (2004) Pressure and shear differentially alter human articular chondrocyte metabolism: a review. *Clin Orthop Relat Res* 427(Suppl):S89–95
- Smith RL, Trindade MCD, Ikenoue T, Mohtai M, Das P, Carter DR, Goodman SB, Schurman DJ (2000) Effects of shear stress on articular chondrocyte metabolism. *Biorheology* 37:95–107
- Soltz MA, Ateshian GA (1998) Experimental verification and theoretical prediction of cartilage interstitial fluid pressurization at an impermeable contact interface in confined compression. *J Biomech* 31:927–934
- Soltz MA, Ateshian GA (2000) A conewise linear elasticity mixture model for the analysis of tension-compression nonlinearity in articular cartilage. *J Biomech Eng* 122:576–586
- Sun YL, Luo ZP, Fertala A, An KA (2002) Direct quantification of the flexibility of type I collagen monomer. *Biochem Biophys Res Commun* 295:382–386
- Taffetani M, Griebel M, Gastaldi D, Klisch SM, Vena P (2014) Poro-viscoelastic finite element model including continuous fiber distribution for the simulation of nanoindentation tests on articular cartilage. *J Mech Behav Biomed Mater* 32:17–30
- Taylor RL, Pister KS, Goudreau GL (1970) Thermomechanical analysis of viscoelastic solids. *Int J Numer Methods Eng* 2:45–59
- Tomic A, Grillo A, Federico S (2014) Poroelastic materials reinforced by statistically oriented fibres—numerical implementation and application to articular cartilage. *IMA J Appl Math* 79:1027–1059
- Topol H, Demirkoparan H, Pence TJ, Wineman A (2014) A theory for deformation dependent evolution of continuous fibre distribution applicable to collagen remodelling. *IMA J Appl Math* 79:947–977
- Tuch DS (2004) Q-ball imaging. *Magn Reson Med* 52:1358–1372
- Wang P, Zhu F, Konstantopoulos K (2010a) Prostaglandin E2 induces interleukin-6 expression in human chondrocytes via cAMP/protein kinase A- and phosphatidylinositol 3-kinase-dependent NF-kappaB activation. *Am J Physiol Cell Physiol* 298:1445–1456
- Wang P, Zhu F, Lee NH, Konstantopoulos K (2010b) Shear-induced interleukin-6 synthesis in chondrocytes: roles of E prostanoïd (EP) 2 and EP3 in cAMP/protein kinase A- and PI3-K/Akt-dependent NF-kappaB activation. *J Biol Chem* 285:24793–24804
- Wilson W, Huyghe JM, van Donkelaar CC (2007) Depth-dependent compressive equilibrium properties of articular cartilage explained by its composition. *Biomech Model Mechanobiol* 6(1–2):43–53
- Wong M, Ponticello M, Kovanen V, Jurvelin JS (2000) Volumetric changes of articular cartilage during stress relaxation in unconfined compression. *J Biomech* 33:1049–1054
- Zhu F, Wang P, Lee NH, Goldring MB, Konstantopoulos K (2010) Prolonged application of high fluid shear to chondrocytes recapitulates gene expression profiles associated with osteoarthritis. *PLoS One* 5:E15174
- Zhu WB, Lai WM, Mow VC (1986) Intrinsic quasi-linear viscoelastic behavior of the extracellular matrix of cartilage. *Trans Orthop Res Soc* 11:407
- Zhu WB, Mow VC, Koob TJ, Eyre DR (1993) Viscoelastic shear properties of articular cartilage and the effects of glycosidase treatments. *J Orthop Res* 11:771–781